

Article

# Carbon Quantum Dots Bridged TiO<sub>2</sub>/CdIn<sub>2</sub>S<sub>4</sub> toward Photocatalytic Upgrading of Polycyclic Aromatic Hydrocarbons to Benzaldehyde

Jiangwei Zhang <sup>1,2,†</sup>, Fei Yu <sup>1,†</sup>, Xi Ke <sup>3</sup>, He Yu <sup>1</sup>, Peiyuan Guo <sup>1</sup>, Lei Du <sup>2</sup> , Menglong Zhang <sup>1,\*</sup> and Dongxiang Luo <sup>2,\*</sup> 

<sup>1</sup> Institute of Hydrogen Energy for Carbon Peaking and Carbon Neutralization, School of Semiconductor Science and Technology, South China Normal University, Foshan 528225, China

<sup>2</sup> School of Chemistry and Chemical Engineering, Huangpu Hydrogen Innovation Center, Guangzhou University, Guangzhou 510006, China

<sup>3</sup> Great Bay Area Branch of Aerospace Information Research Institute, Chinese Academy of Sciences, Guangzhou 510530, China

\* Correspondence: mlzhang@m.scnu.edu.cn (M.Z.); luodx@gdut.edu.cn (D.L.)

† These authors contributed equally to this work.

**Abstract:** Conversion of hazardous compounds to value-added chemicals using clean energy possesses massive industrial interest. This applies especially to the hazardous compounds that are frequently released in daily life. In this work, a S-scheme photocatalyst is optimized by rational loading of carbon quantum dots (CQDs) during the synthetic process. As a bridge, the presence of CQDs between TiO<sub>2</sub> and CdIn<sub>2</sub>S<sub>4</sub> improves the electron extraction from TiO<sub>2</sub> and supports the charge transport in S-scheme. Thanks to this, the TiO<sub>2</sub>/CQDs/CdIn<sub>2</sub>S<sub>4</sub> presents outstanding photoactivity in converting the polycyclic aromatic hydrocarbons (PAHs) released by cigarette to value-added benzaldehyde. The optimized photocatalyst performs 87.79% conversion rate and 72.76% selectivity in 1 h reaction under a simulated solar source, as confirmed by FT-IR and GC-MS. A combination of experiments and theoretical calculations are conducted to demonstrate the role of CQDs in TiO<sub>2</sub>/CQDs/CdIn<sub>2</sub>S<sub>4</sub> toward photocatalysis.

**Keywords:** carbon quantum dots; photocatalysis; degradation; polycyclic aromatic hydrocarbons



**Citation:** Zhang, J.; Yu, F.; Ke, X.; Yu, H.; Guo, P.; Du, L.; Zhang, M.; Luo, D. Carbon Quantum Dots Bridged TiO<sub>2</sub>/CdIn<sub>2</sub>S<sub>4</sub> toward Photocatalytic Upgrading of Polycyclic Aromatic Hydrocarbons to Benzaldehyde. *Molecules* **2022**, *27*, 7292. <https://doi.org/10.3390/molecules27217292>

Academic Editors: Michael Moustakas, Ilektra Sperdouli and Georgia Ouzounidou

Received: 29 September 2022

Accepted: 23 October 2022

Published: 27 October 2022

**Publisher's Note:** MDPI stays neutral with regard to jurisdictional claims in published maps and institutional affiliations.



**Copyright:** © 2022 by the authors. Licensee MDPI, Basel, Switzerland. This article is an open access article distributed under the terms and conditions of the Creative Commons Attribution (CC BY) license (<https://creativecommons.org/licenses/by/4.0/>).

## 1. Introduction

In fossil industrial societies, environmental pollution is closely related to the rapid progress of modern industry [1–3]. Among the kinds of pollutants, more and more public attention has been paid to the ecological environment change caused by organic pollutants [4,5]. In domestic sewage, organic pollutants usually include benzene compounds (Polychlorinated biphenyls) [6], formaldehyde [7], tobacco tar (PAHs) [8]. When tobacco and cigarette paper are insufficiently burned, the tobacco tars with polycyclic aromatic hydrocarbons (PAHs) as major pollutants may be formed [9]. PAHs are aromatic hydrocarbons with two or more fused aromatic rings, which can be combined in two forms, the non-viscous ring type and the viscous ring type [10]. It is well known that PAHs in the environment will be particularly harmful to human health [11], causing a variety of hazards to the respiratory system and circulatory system. Currently, the general methods of dealing with PAHs in pollutants include biological degradation [12], adsorption process [10] and photocatalytic degradation [13]. Although biodegradation is environmentally friendly, it can be restricted by various factors such as temperature, pH and microbial adaptations, and adsorption treatment prefers transferring organic pollutants to the adsorbent rather than reducing the concentration of it [14]. In contrast, semiconductor photocatalysis is considered as an appealing method for breaking down toxic compounds into non-toxic carbon dioxide and water under mild conditions [15]. Semiconductor-based photocatalytic

reactions are environment friendly, having a high surface area, low cost and high modification, etc. [16,17]. It is worth noting that there is still little research on tobacco tar via photocatalytic degradation.

In recently years, abundant types of photocatalysts have been playing an important role, including ZnO [18], SrTiO<sub>3</sub> [19], SnO<sub>2</sub> [20], Bi<sub>2</sub>S<sub>3</sub> [21], and so on. Unfortunately, the narrow absorption spectra and unsatisfactory photocatalytic performance limit their application. Thus, exploring highly active at the range of visible-light-driven photocatalysts is still a constant pursuit of researchers.

Titanium oxide (TiO<sub>2</sub>) is a classical semiconductor with favorable thermal and chemical stability [22,23]. However, limited by the wide band gap (3.2 eV) [24,25] and rapid photo-generated electron-hole recombination, the solar energy utilization of TiO<sub>2</sub> is typically inefficient, resulting in a low photocatalytic efficiency [26,27]. Therefore, researchers have developed a variety of strategies for enhancing the photocatalytic performance of TiO<sub>2</sub>, such as precious metal deposition, pigment sensitization and metal ion doping, etc. [28]. Comparing with the above strategies, the construction of heterojunctions has been demonstrated to be an effective way for tuning the absorption and manipulating the charge separation [29]. For instance, a TiO<sub>2</sub>/CdIn<sub>2</sub>S<sub>4</sub> hierarchical nano hetero-structure photocatalyst demonstrated an ~5.5 times higher in hydrogen production from water compared to bare TiO<sub>2</sub> under visible light [30].

CdIn<sub>2</sub>S<sub>4</sub>, as a ternary metal chalcogenide compound, is equipped with an appropriate band gap (2.03–2.26 eV) and photoredox potential, promoting the light capture efficiency at visible light range [31,32]. Considering these advantages, CdIn<sub>2</sub>S<sub>4</sub> has been reported to contribute to photocatalytic degradation of pollutants [33], water splitting [31], and carbon dioxide (CO<sub>2</sub>) photoreduction [34]. However, due to the photoinduced hole self-oxidation of bare CdIn<sub>2</sub>S<sub>4</sub> and the rapid recombination of photoexcited charges, the practical application suffers a huge impediment [35]. In recent years, combining semiconductor materials with CdIn<sub>2</sub>S<sub>4</sub> has been one of the approaches to solving the transfer direction of photo-generated carriers [36]. Moreover, the charge transfer rate of the composite photocatalyst system is closely related to the electrical conductivity between the material interfaces, which directly affects its catalytic activity [37]. Therefore, the introduction of materials with good electrical conductivity can facilitate the charge transfer of photoexcited semiconductors and co-catalysts.

Carbon quantum dots (CQDs), as a novel carbon nano material, are universally employed in various fields because of their excellent properties [38]. In the field of photocatalysis, CQDs have been used to modify binary semiconductor nano materials for its efficient electronic transmission capability [39]. For instance, Liang et al. showed a novel Z-scheme g-C<sub>3</sub>N<sub>4</sub>/CQDs/CdIn<sub>2</sub>S<sub>4</sub> heterojunction showing an improvement of ~1.5 times higher photocatalytic degradation than g-C<sub>3</sub>N<sub>4</sub>/CdIn<sub>2</sub>S<sub>4</sub> composite [40]. Pei et al. synthesized the ternary NiS/CQDs/ZnIn<sub>2</sub>S<sub>4</sub> nanocomposite by a simple hydrothermal method. Compared with NiS/ZnIn<sub>2</sub>S<sub>4</sub> heterojunction, the hydrogen production efficiency was more than 1.75 times [37]. Looking at these facts, it can be anticipated that CQDs play a crucial role in the charge transfer between TiO<sub>2</sub> and CdIn<sub>2</sub>S<sub>4</sub>.

In this study, an active photocatalyst was developed by hydrothermal method that involves TiO<sub>2</sub>/CdIn<sub>2</sub>S<sub>4</sub> heterojunction being modified with CQDs as bridge to improve the electron transport efficiency. Meanwhile, we investigated the effect of different ratios of CQDs on the photocatalytic performance of the TiO<sub>2</sub>/CQDs/CdIn<sub>2</sub>S<sub>4</sub> heterojunction to obtain the optimum fabrication parameters. The composition, structure, morphology and optical properties of the prepared heterojunction were analyzed thoroughly. PAHs, a typical hazardous organic chemical in products of incomplete combustion tobacco, was chosen as the typical pollutant in tobacco tar. The photocatalytic degradation mechanism of PAHs by prepared heterojunction, the electron transfer and decomposition products were analyzed in detail.

## 2. Experimental

### 2.1. Chemicals

Thioacetamide ( $C_2H_5NS$ , Macklin<sup>®</sup>99% purity), indium nitrate hydrate, ( $InH_3O_9 \cdot xH_2O$ , Aladdin<sup>®</sup>99% purity), cadmium nitrate tetrahydrate ( $Cd(NO_3)_2 \cdot 4H_2O$ , Aladdin<sup>®</sup>99% purity), citric acid ( $C_6H_8O_7$ , Macklin<sup>®</sup>98% purity), urea ( $CH_4N_2O$ , Aladdin<sup>®</sup>99.5% purity), acenaphthylene (ANY) ( $C_{12}H_8$ , Aladdin<sup>®</sup>97% purity), titanium oxide, rutile (60 nm) ( $TiO_2$ , Macklin<sup>®</sup>99.8% purity) were used in this study.

### 2.2. Synthesis of CQDs Colloidal Solution

In a typical synthesis, 4 g of citric acid (AC) and 4 g of urea were added to 80 mL of distilled water and the prepared solution was stirred for 15 min at 600 rpm. Then, the mixture solution was transferred into a Teflon-lined cylinder in a stainless-steel autoclave for hydrothermal synthesis of CQDs at 120 °C for 12 h. The brownish-green final CQD colloidal solution was collected after cooling at room temperature naturally [41].

### 2.3. Preparation of the $TiO_2/CdIn_2S_4$ Photocatalyst

The hydrothermal method was used to synthesize the  $TiO_2/CdIn_2S_4$  photocatalysts. The 80 mg  $TiO_2$  (60 nm), 0.308 g cadmium nitrate ( $Cd(NO_3)_2 \cdot 4H_2O$ ), 0.600 g indium nitrate ( $In(NO_3)_3 \cdot 3H_2O$ ) and 0.302 g thioacetamide ( $C_2H_5NS$ ) were dissolved in 70 mL of distilled water. Then, the solution was taken to be stirred for about 4 h with the Teflon magneton. After that, the mixed solution was sent to a 100 mL Teflon-lined autoclave with hydrothermal method at 120 °C for 12 h. After cooling to room temperature, the as-prepared photocatalyst was washed with distilled water and ethanol three times and dried at 70 °C for 4 h.

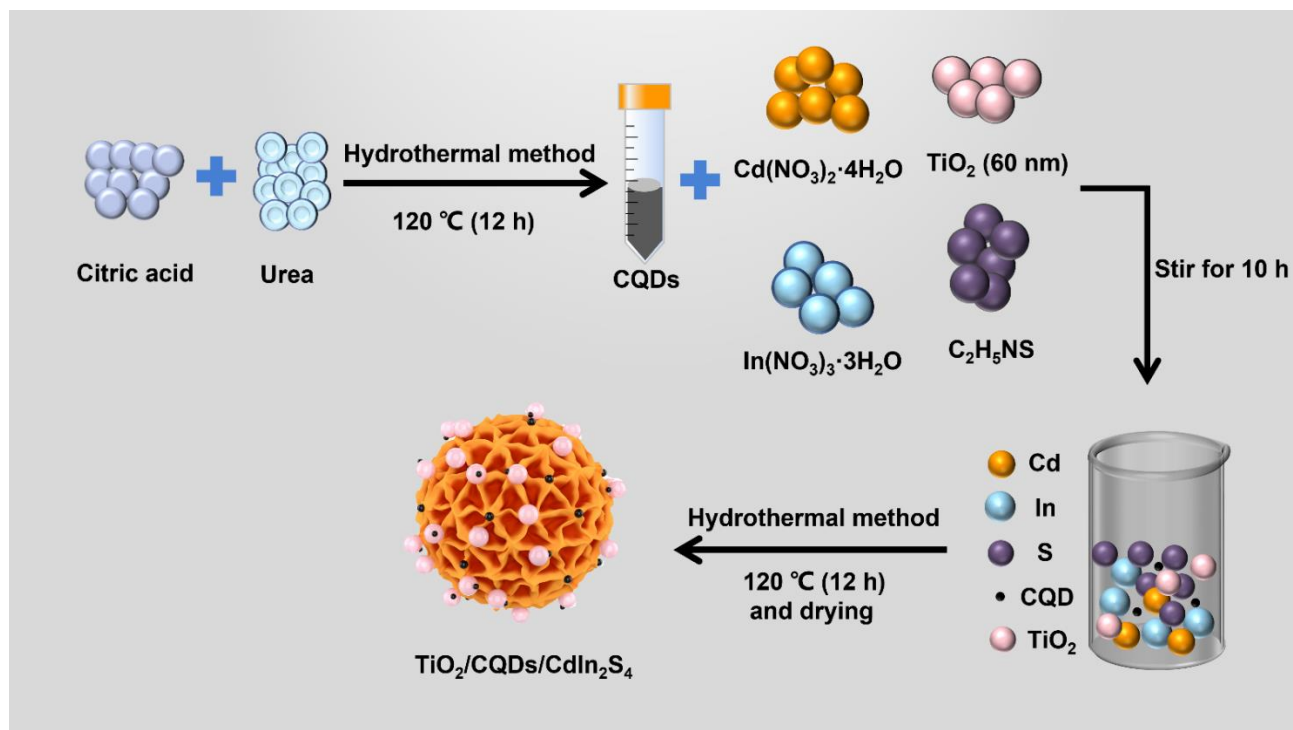
### 2.4. Preparation of the $TiO_2/CQDs/CdIn_2S_4$ Photocatalysts

The  $TiO_2/CQDs/CdIn_2S_4$  photocatalysts were prepared by the hydrothermal method. In detail, 0.154 g cadmium nitrate ( $Cd(NO_3)_2 \cdot 4H_2O$ ), 0.300 g indium nitrate ( $In(NO_3)_3 \cdot 3H_2O$ ) and 0.151 g thioacetamide ( $C_2H_5NS$ ) were dissolved in 30 mL of distilled water (as solution A). Meanwhile, the CQDs dispersion divided into different gradients from 250  $\mu$ L to 2500  $\mu$ L was dripped in 40 mL distilled water before 40 mg  $TiO_2$  was added and stirred for 1 h (as solution B). Then, solution A was slowly added into solution B to obtain solution C. After being stirred for 10 h, solution C was subjected to a 100 mL Teflon-lined autoclave and maintained at 120 °C for 12 h. The obtained final product was washed with distilled water and ethanol three times and dried at 70 °C for 4 h [30]. The scheme for the synthesis is presented in Scheme 1.

### 2.5. Characterization

The crystalline phase and crystalline size of the samples were analyzed by using an X-ray powder diffraction (XRD) technique (Rigaku Corporation, Japan) with  $Cu K\alpha 1$  radiation ( $\lambda = 1.541866 \text{ \AA}$ ), scanning angle from 10° to 80° (2 $\theta$ ). The morphology and structure of the  $TiO_2/CQDs/CdIn_2S_4$ /photocatalysts were measured by transmission electron microscope (TEM, Japan-JEOL-JEM 2100F) and scanning electron microscopy (SEM, American-FEI-Quanta FEG 250). Transmission electron microscope was employed for the elemental mapping (Japan-JEOL-JEM 2100 F). X-ray photoelectron spectroscopy (XPS) was measured by Thermo SCIENTIFIC ESCALAB 250Xi (ThermoFisher Nexsa, America, X-ray source-Al  $K\alpha$  ray ( $h\nu = 1486.8 \text{ eV}$ ) the work function: 4.97 eV). The FT-IR spectra in the range from 400 to 4000  $cm^{-1}$  was analyzed by a thermogravimetric spectrum instrument (America-Agilent-7890). Electron paramagnetic resonance (EPR) measurements was obtained using a CW-EPR Bruker spectrometer (Germany Bruker-A200). Spectrum measurement system was applied to collect. The UV-vis absorption spectroscopy of the samples (DH-2000-BAL) and the steady-state photoluminescence (PL) spectra of the photocatalysts were recorded by fluorescence spectrometer (QE65000-FL). The gas chromatography-mass spectrometer (GC-MS) was used to analyze the photocatalytic degradation of PAHs. In this experiment,

the temperature is programmed as follows: maintain the initial 45 °C for 1.5 min; 10 °C/min to 200 °C for 1 min; 2.5 °C/min to 250 °C for 1 min; 4 °C/min to 280 °C for 3 min; 5 °C/min to 300 °C and hold for 10 min.



**Scheme 1.** Synthesis scheme for  $\text{TiO}_2/\text{CQDs}/\text{CdIn}_2\text{S}_4$  photocatalysts.

### 2.6. Photocatalytic Experiment

The photocatalytic activities of  $\text{TiO}_2/\text{CQDs}/\text{CdIn}_2\text{S}_4$  (different ratio of CQDs),  $\text{TiO}_2/\text{CdIn}_2\text{S}_4$  and bare  $\text{CdIn}_2\text{S}_4$  were studied by comparative absorption spectra, and the optimal proportion of CQDs in the photocatalyst was determined. The 50 mg of the as-prepared photocatalysts was added in the substrate solution. The 300 W Xe lamp was used as the light source to provide UV or visible light (long-pass filter ( $>400$  nm)). To evaluate the photocatalytic performance for cigarette tar degradation, acenaphthylene (ANY) was employed for the photocatalytic experiments, due to its predominant content in cigarette tar. The substrate was dissolved in toluene solvent at 1 mg/L, and the amount of the photocatalyst was 0.5 g/L. Before the illumination, the mixture was stirred with Teflon magneton for 30 min under dark conditions to ensure uniform mixing of photocatalyst and polycyclic aromatic hydrocarbon molecules.

To calculate density functional theory (DFT) within the generalized gradient approximation (GGA) using the PBE [42] formulation, Vienna Ab Initio Package (VASP) was exploited [43,44]. In this study, we performed the projected augmented wave (PAW) potentials for describing the ionic cores and to account for valence electrons, working on 450 eV kinetic energy cutoffs [45,46]. With Gaussian smearing, partial occupancies of the Kohn–Sham orbitals were allowed at a width of 0.05 eV. The on-site corrections (DFT+U) were subjected to the 3D electron of Ti atoms ( $U_{\text{eff}} = 4.5$  eV). Electronic energy was identified as self-consistent when the change in energy was less than  $10^{-5}$  eV. The geometry optimization was known as convergent when the force change was less than 0.02 eV/Å. Grimme’s DFT-D3 approach was employed to illustrate the dispersion interactions.

We determined  $a = b = 3.858$  Å and  $c = 9.652$  Å for anatase  $\text{TiO}_2$  unit cells when employing a  $10 \times 10 \times 4$  Monkhorst-Pack k-point grid for Brillouin zone sampling. For Brillouin zone sampling, the equilibrium lattice constant of cubic  $\text{CdIn}_2\text{S}_4$  is  $a = 10.920$  Å, in the presence of a  $2 \times 2 \times 2$  Monkhorst-Pack k-point grid. Hexagonal graphene unit

cells isolated by a vacuum layer of 15 Å depth were optimized for equilibrium lattice constants, being regarded as  $a = 2.468$  Å, when employing a  $15 \times 15 \times 15$  Monkhorst-Pack k-point grid for Brillouin zone sampling. After that, two heterojunction surface models were constructed. The first was a heterojunction surface model based on  $\text{TiO}_2/\text{CdIn}_2\text{S}_4$  (101). The part of  $\text{CdIn}_2\text{S}_4$  has a  $p$  ( $1 \times 2$ ) periodicity in the X and Y directions and one stoichiometric layer in the Z direction; the  $\text{TiO}_2$  (101) part has a  $p$  ( $1 \times 6$ ) periodicity in the X and Y directions and two stoichiometric layers in the Z direction; the  $\text{TiO}_2/\text{CdIn}_2\text{S}_4$  (101) slab was added with a vacuum layer in the Z direction at the depth of 15 Å in order to separate the surface slab from its periodic duplicates. The second heterojunction model was built by adding a graphene monolayer with a  $(4 \times 5\sqrt{3})$  periodicity between the two parts of model 1. During structural optimizations, the  $\Gamma$  point in the Brillouin zone was used for k-point sampling, and the bottom stoichiometric layer of the  $\text{TiO}_2$  (101) part was fixed while the rest were allowed to fully relax.

### 3. Result and Discussions

#### 3.1. Characterizations of Structure and Morphology

The morphology and microstructure of the as-prepared photocatalysts were initially checked by scanning electron microscope (SEM). As shown in Figure 1A,  $\text{TiO}_2$  presented a spherical shape with uniform particle size of ca. 65 nm. After coupling  $\text{TiO}_2$  with  $\text{CdIn}_2\text{S}_4$  through a hydrothermal method, the stacked nanospheres with wrinkles were monitored (Figure 1B), which is consistent with the previous reports [32,47]. The morphology can be attributed to that the anisotropy of  $\text{CdIn}_2\text{S}_4$  drives a directional growth, leading to the presence of nanosheets and subsequent self-assembly. While, the decoration of carbon quantum dots (CQDs) on  $\text{TiO}_2/\text{CdIn}_2\text{S}_4$  resulted in no obvious morphological changes as observed by SEM, which can be explained by the small size of the CQDs (Figure 1C) [48].

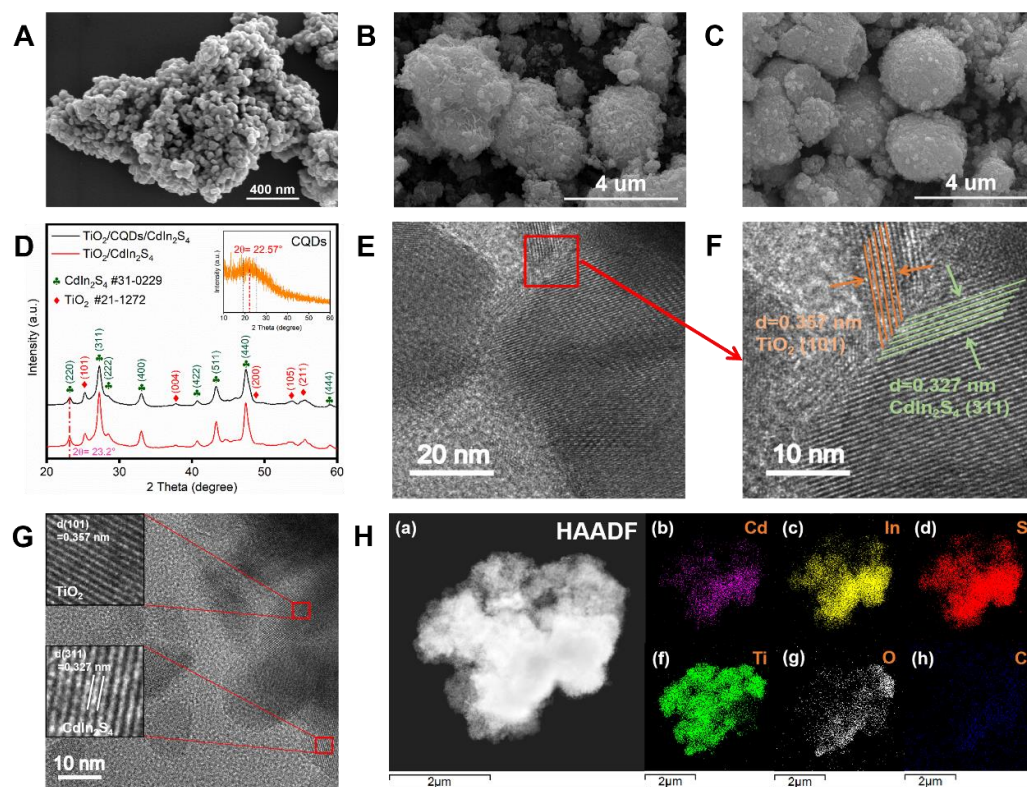


**Figure 1.** SEM images of (A) as-prepared  $\text{TiO}_2$ ; (B)  $\text{TiO}_2/\text{CdIn}_2\text{S}_4$ ; (C)  $\text{TiO}_2/\text{CQDs}/\text{CdIn}_2\text{S}_4$ ; (D) PXRD patterns of  $\text{TiO}_2/\text{CdIn}_2\text{S}_4$  and  $\text{TiO}_2/\text{CQDs}/\text{CdIn}_2\text{S}_4$ ; (E–G) TEM images of  $\text{TiO}_2/\text{CQDs}/\text{CdIn}_2\text{S}_4$  at different magnifications and locations; (H) TEM-EDS elemental mapping of  $\text{TiO}_2/\text{CQDs}/\text{CdIn}_2\text{S}_4$ .

To confirm the phase and crystal structures of the as-prepared samples, powder X-ray diffraction (PXRD) (Figures 1D and S1) analysis was performed. On the one hand, the main diffraction peaks located at  $2\theta = 23.15^\circ, 27.24^\circ, 33.00^\circ, 40.73^\circ, 43.31^\circ$  and  $47.41^\circ$  can be indexed to cubic crystal structure of  $\text{CdIn}_2\text{S}_4$  (JCPDS#27-0060), corresponding to the indices of (220), (311), (400), (422), (511) and (440) planes, respectively [49,50]. On the other hand, the diffraction peaks in  $\text{TiO}_2/\text{CQDs}/\text{CdIn}_2\text{S}_4$  composite exhibit a standard phase of tetragonal  $\text{TiO}_2$  (JCPDS#21-1272) with the lattice (101), (004), (200), (105) and (211) [30]. In addition, CQDs (top right) showed a broad peak centered at  $2\theta = 22.57^\circ$  with low intensity owing to the small size, which is consistent with the previous reports [48,51–53]. Thus, the (220) plane of  $\text{CdIn}_2\text{S}_4$  at  $2\theta = 23.2^\circ$  in  $\text{TiO}_2/\text{CQDs}/\text{CdIn}_2\text{S}_4$  did not alter significantly compared with  $\text{TiO}_2/\text{CdIn}_2\text{S}_4$  due to the low intensity of CQDs characteristic peak. The crystal size of CQDs is evaluated based on the PXRD patterns using Debye–Scherrer equation [53–56], which is capable of calculating the size of nanocrystals based on the X-ray diffraction features, regardless of the aggregation of these nanocrystals. Meanwhile, the full width at half maximum (FWHM) of as-prepared CQDs is measured to be  $546.01 \times 10^{-4}$  rad, suggesting an ultra-small size of ca. 2.5615 nm (Table 1), confirming that the synthesized samples were quantum dots with the unique property of quantum dots, whose size ranges from 1 to 10 nm. As seen in Figure 1D, in comparison to  $\text{TiO}_2/\text{CdIn}_2\text{S}_4$ ,  $\text{TiO}_2/\text{CQDs}/\text{CdIn}_2\text{S}_4$  presents no significant change, which is ascribed to the weak XRD signal of CQDs.

**Table 1.** The crystal sizes of the photocatalysts and CQDs calculated by Debye–Scherrer equation.

Sample	$\beta$ (rad)	$2\theta$ ( $^\circ$ )	$D_{311}$ (nm)
$\text{TiO}_2/\text{CQDs}/\text{CdIn}_2\text{S}_4$	$86.873 \times 10^{-4}$	27.181	16.275
$\text{TiO}_2/\text{CdIn}_2\text{S}_4$	$75.534 \times 10^{-4}$	27.220	18.681
CQDs	$546.01 \times 10^{-4}$	22.570	2.5615

Transmission electron microscopy (TEM) was employed to further demonstrate the microscopic structure of  $\text{TiO}_2/\text{CQDs}/\text{CdIn}_2\text{S}_4$ . The uniformly distributed lattice fringes in Figure 1E,F clearly present the intimate interfacial contact between  $\text{TiO}_2$  and  $\text{CdIn}_2\text{S}_4$ . The lattice spacings of 0.357 nm and 0.327 nm are exhibited in Figure 1F,G, which correspond to (101) planes of the tetragonal phase of  $\text{TiO}_2$  and (311) planes of the cubic phase of  $\text{CdIn}_2\text{S}_4$  [33,57], respectively; this is in full accord with the PXRD results. Based on the crystal parameters of  $\text{TiO}_2$  and  $\text{CdIn}_2\text{S}_4$ , the lattice mismatch can be obtained as  $\Delta d/d\text{TiO}_2 = 8\%$ . The small lattice mismatch typically indicates rapid transfer of photogenerated carriers between interfaces of  $\text{TiO}_2/\text{CdIn}_2\text{S}_4$  due to the lower interfacial trap state [58]. Next, energy dispersive spectra (EDS) mapping was employed to investigate the elemental composition and distribution of  $\text{TiO}_2/\text{CQDs}/\text{CdIn}_2\text{S}_4$  photocatalysts. As shown in Figure 1H, carbon can be clearly detected to be evenly distributed in the whole  $\text{TiO}_2/\text{CdIn}_2\text{S}_4$  region. In addition, Cd, In, S, Ti and O elements were also confirmed from the sample, which can correspond to the elemental composition of  $\text{TiO}_2/\text{CQDs}/\text{CdIn}_2\text{S}_4$  photocatalysts. For further confirming the content difference of CQDs between  $\text{TiO}_2/\text{CQDs}/\text{CdIn}_2\text{S}_4$  and  $\text{TiO}_2/\text{CdIn}_2\text{S}_4$ , Figures S5 and S6 and Table S1 show that C element was not found in  $\text{TiO}_2/\text{CdIn}_2\text{S}_4$  photocatalysts.

### 3.2. Band Structure of $\text{TiO}_2/\text{CQDs}/\text{CdIn}_2\text{S}_4$ Photocatalysts

Figure 2A illustrates the UV-Vis diffuse reflectance spectrum (DRS) of bare  $\text{TiO}_2$ ,  $\text{CdIn}_2\text{S}_4$ ,  $\text{TiO}_2/\text{CdIn}_2\text{S}_4$  and  $\text{TiO}_2/\text{CQDs}/\text{CdIn}_2\text{S}_4$  photocatalysts. The tetragonal  $\text{TiO}_2$  exhibited a typical absorption edges at 387 nm, situated in the absorption range of ultraviolet light [59]. Meanwhile, the absorption edge of  $\text{CdIn}_2\text{S}_4$  can be observed at 610 nm corresponding to the band gap energy of 2.03 eV [49]. Furthermore, the loading of  $\text{CdIn}_2\text{S}_4$  on  $\text{TiO}_2$  lead to a light absorption range of the composite extended to the visible region comparing to pristine  $\text{TiO}_2$  [30,60]. After the introduction of CQDs,  $\text{TiO}_2/\text{CQDs}/\text{CdIn}_2\text{S}_4$  presented a slightly enhanced absorption capability in range from 600 to 900 nm, which can

be attributed to the narrow band gap energy of CQDs [48]. The valence state of the samples was evaluated by X-ray photoelectron spectroscopy (XPS), from which the characteristic binding energies of Cd (3d), In (3d), S (2p) and Ti (2p) were in good agreement with the rational valence state of the composite (Figure 2B–E). As shown in Figure 2F, the XPS profile of O 1s in the initial state presented three peaks located at 529.67, 521.97 and 533.02 eV, corresponding to the lattice oxygen, adsorbed oxygen [61] and surface hydroxyl, respectively [62–64]. Under UV illumination, we observed a dramatically reduced O 1s (533.50 eV) peak corresponding to the surface hydroxyl (Figure 2F). Considering the reductivity of hydroxyl species and that the valence of  $\text{TiO}_2$  was composed by O orbitals, this result indicates that the O in  $\text{TiO}_2$  featured highly active oxidation sites in  $\text{TiO}_2/\text{CQDs}/\text{CdIn}_2\text{S}_4$ , possibly as a S-scheme structure (Figure S6) [60], where the hydroxyl species were oxidized by the photo-generated holes in the valence band of  $\text{TiO}_2$ . Based on the valence plots depicted in the Figure S2, the valence band ( $E_{\text{VB}}$ ) of the  $\text{CdIn}_2\text{S}_4$  and  $\text{TiO}_2$  were calculated to be 0.56 eV and 2.23 eV [65]. Meanwhile, due to the band gap energy ( $E_g$ ) of the  $\text{CdIn}_2\text{S}_4$  ( $E_g = 2.02$  eV) and  $\text{TiO}_2$  ( $E_g = 3.20$  eV) shown in Figure 2A, the band structure of the S-scheme of  $\text{TiO}_2/\text{CQDs}/\text{CdIn}_2\text{S}_4$  and type-II of  $\text{TiO}_2/\text{CdIn}_2\text{S}_4$  were constructed in Figure 2G. Notably, compared with the type-II, the photogenerated electrons in CB of  $\text{TiO}_2$  and the holes produced in the VB of  $\text{CdIn}_2\text{S}_4$  are inclined to recombine on the CQDs bridge during the photocatalytic reaction of S-scheme under the Coulombic attraction between electrons and holes [66]. Since more holes are accumulated in the VB of  $\text{TiO}_2$ , the oxidation ability of the S-scheme photocatalyst becomes stronger.

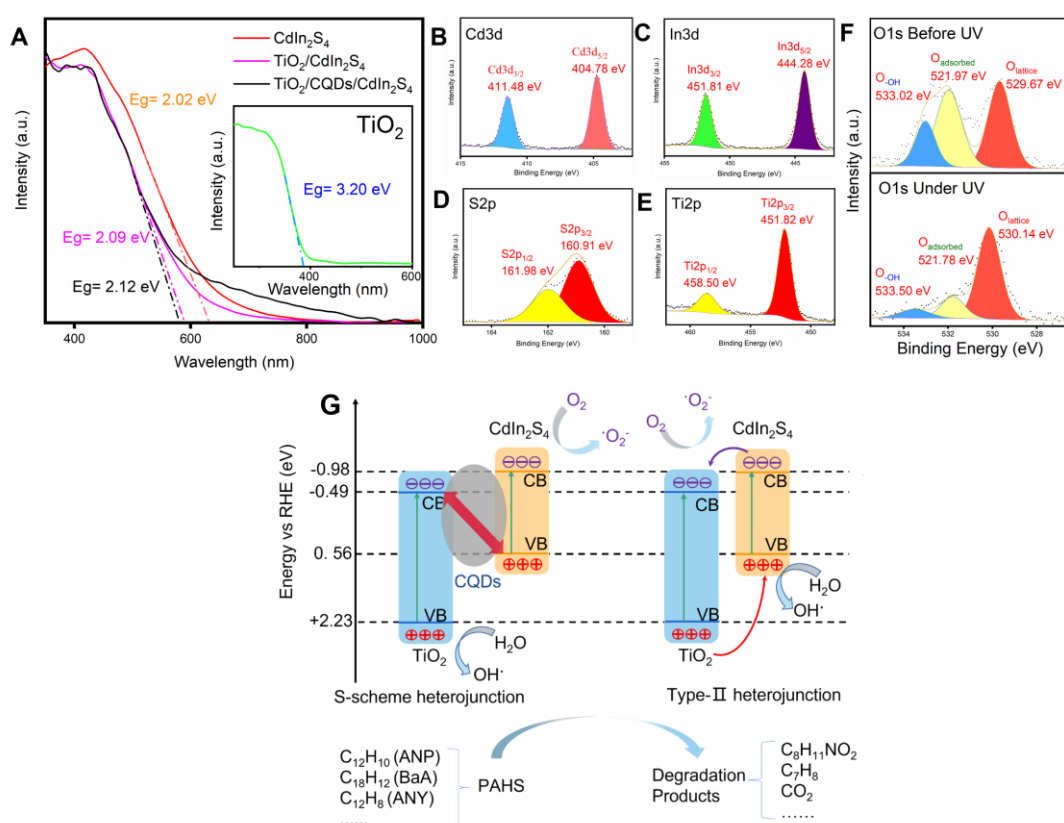


**Figure 2.** (A) UV-vis DRS of  $\text{CdIn}_2\text{S}_4$ ,  $\text{TiO}_2/\text{CdIn}_2\text{S}_4$  and  $\text{TiO}_2/\text{CQDs}/\text{CdIn}_2\text{S}_4$ ; (B–E) XPS spectra of the main elements in  $\text{TiO}_2/\text{CQDs}/\text{CdIn}_2\text{S}_4$ ; (F) In-situ XPS spectra of O 1s orbital in  $\text{TiO}_2/\text{CQDs}/\text{CdIn}_2\text{S}_4$ , the data was collected with/without 365 nm irradiation; (G) The band position and charge transfer of S-scheme photocatalytic reaction process of  $\text{TiO}_2/\text{CQDs}/\text{CdIn}_2\text{S}_4$  and the type-II photocatalytic reaction process of  $\text{TiO}_2/\text{CdIn}_2\text{S}_4$  under illumination.

### 3.3. Influence of S Defects Formation

Figure 3A presents the cubic spinel structure  $\text{CdIn}_2\text{S}_4$  indexing to the space group FD-3m (No.227), where the purple, magenta and yellow balls represent the Cd, In and S atoms, respectively [67]. The In atom is connected to six S atoms, forming the In-S octahedral structure. The blue and red balls represent the Ti and O atoms, which constitutes the tetragonal  $\text{TiO}_2$ . The CQDs serve as a bridge to conduct electricity between  $\text{TiO}_2$  and  $\text{CdIn}_2\text{S}_4$  (Figure 3B). To further investigate the roles of CQDs in  $\text{TiO}_2/\text{CQDs}/\text{CdIn}_2\text{S}_4$ , the density of state (DOS) was conducted using first-principle calculations. As depicted in Figure 3C, the shallow trap states that primarily consisted of S (3p), O (2p) and In (5p) orbitals were projected, which are consistent with the pristine component (Figure S3). A peak corresponding to S 3p orbital at the Fermi level ( $E-E_f = 0$  eV) indicates the presence of S defects [68]. The generation of surface sulfur vacancies typically leads to the accumulation of charges on adjacent Cd and In atoms, which may serve as highly active sites for intermediate chemisorption during photocatalytic degradation. Additionally, with respect to  $\text{TiO}_2/\text{CdIn}_2\text{S}_4$  (Figure 3C), after the introduction of CQDs (Figure 3D), the DOS of valence band orbital of O atom shows a clear downward trend due to the increased electron extraction from O, suggesting an enhancement in the oxidation capacity of  $\text{TiO}_2$  [69], which is consistent with our in-situ XPS result. Furthermore, in consideration of the critical role of radicals in the photocatalytic process, electron paramagnetic resonance (EPR) was applied to monitor the influence of CQDs on radical generation under illumination. The EPR results in Figure S4 confirmed that the samples with/without are both capable of producing superoxide and hydroxyl radicals under illumination, and the radical concentration generated from the sample with CQDs is slightly higher than that of the control group.

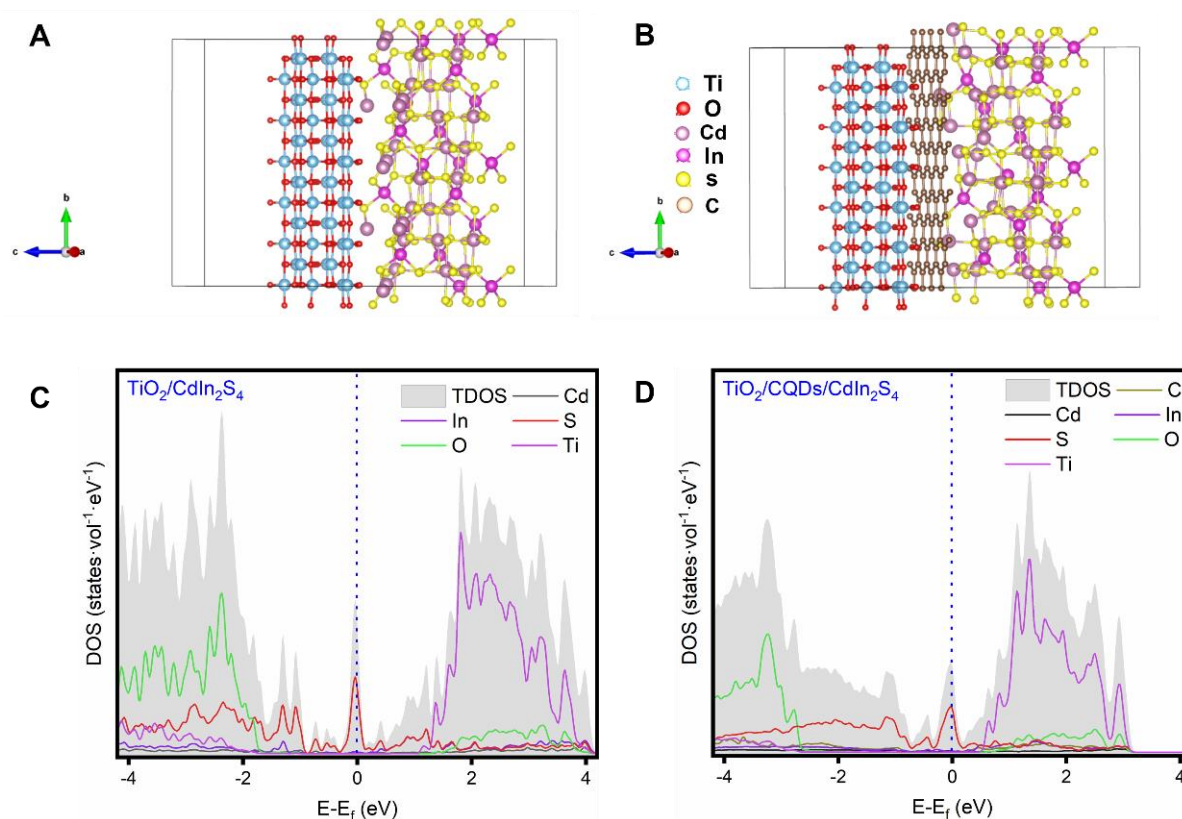


**Figure 3.** The crystal structures of (A)  $\text{TiO}_2/\text{CdIn}_2\text{S}_4$  and (B)  $\text{TiO}_2/\text{CQDs}/\text{CdIn}_2\text{S}_4$ ; density of states of (C)  $\text{TiO}_2/\text{CdIn}_2\text{S}_4$  and (D)  $\text{TiO}_2/\text{CQDs}/\text{CdIn}_2\text{S}_4$ .

### 3.4. Influence of CQDs Content on Oxidation Performance

The as-prepared photocatalysts were exploited to degrade PAHs from cigarette tar to produce valuable products. First, 10 mg of the as-prepared photocatalysts was added in PAHs substrate, then the reaction was conducted under  $100 \text{ mW cm}^{-2}$  simulated solar source with AM 1.5 G filter. A combination of gas chromatography-mass spectroscopy (GC-MS), Fourier-transform infrared spectroscopy (FT-IR) and UV-vis DRS were employed to evaluate the degradation rate and products. Before the photocatalytic tests, the PAHs substrate and photocatalysts were initially mixed and stirred under dark conditions for 30 min to achieve adsorption equilibrium, during which we monitored no obvious change in UV-vis DRS.

In terms of the photocatalytic performance, the ratio of CQDs in  $\text{TiO}_2/\text{CQDs}/\text{CdIn}_2\text{S}_4$  presented a strong impact on the photocatalytic degradation rate over PAHs (Figure 4A). Namely, the photocatalytic activity increased with the increased ratio of CQDs, it and reached the zenith at 20 to 30 mg/L, which was then followed with a decreased activity. This may be due to the overloading of CQDs leading to a reduced charge transfer efficiency between  $\text{TiO}_2$  and  $\text{CdIn}_2\text{S}_4$ , which suppresses the S-scheme features of the photocatalysts. To further optimize the ratio of CQDs, we tested the range of CQDs between 20 to 25 mg/L, in which the 23 mg/L presented a degradation rate up to 78.5% (Figure 4B). As illustrated in Figure 4C, the color of the substrate changed from the initial brown to a transparent colorless solvent in 1 h photocatalytic process. In addition to the loss of color, a blue shift of the absorption maximum (from 430 to 385 nm) was also monitored during the photocatalytic reaction (Figure 4D). As it is known that the molecular structure can be reflected by the absorption spectra, to be specific, a decreased number of conjugated carbon-carbon double bonds typically result in an absorption spectrum with a shorter wavelength [70]. In our case, the blue shift suggests that carbon-carbon double bonds in PAHs is possibly destroyed during the photocatalytic degradation. The comparison of the degradation performances among the serials of samples were exhibited in Figure 4E, particularly, the loading of rational content of CQDs between  $\text{TiO}_2$  and  $\text{CdIn}_2\text{S}_4$  dramatically improved the photocatalytic activity, comparing to the control group (from 45.81 to 78.50%), suggesting the photoactivity can be efficiently promoted by adding CQDs. Furthermore, the PAHs degradation performance was compared as shown in Table 2. Besides, the stability of  $\text{TiO}_2/\text{CQDs}/\text{CdIn}_2\text{S}_4$  was checked by repeating the experiments 3 times using the recycled samples (Figure 4F) Comparing to the initial cycle, ca. 7.2% photoactivity loss was observed in the second cycle. Meanwhile, for further confirming the stability of photocatalysts in PAHs degradation, as shown in Figure S7, 97.6% samples were retained in the two  $\text{TiO}_2/\text{CQDs}/\text{CdIn}_2\text{S}_4$  sample groups after 5 h photocatalytic degradation. While in the third cycle, the photoactivity loss was less than 2%, relative to the second cycle. As confirmed by PXRD (Figure 4G,H), the characteristic patterns of  $\text{TiO}_2/\text{CQDs}/\text{CdIn}_2\text{S}_4$  basically remain the same after 3 reaction cycles. As depicted in Figure S8, the hot filtration test was conducted to confirm the compatibility of  $\text{TiO}_2/\text{CQDs}/\text{CdIn}_2\text{S}_4$  photocatalysts [71]. After 10 min of reaction under simulated sunlight (degradation of 65.2% PAHs), the photocatalyst was removed and filtered. Then the filtrate was illuminated for another 50 min under the same condition with no significant increase in degradation, confirming that no leaching of the photocatalyst components emerged [72]. Meanwhile, the ICP-MS analysis was performed to reveal the metal leaching of the pure filtrate [73]. The contents of Cd, In and Ti were 0.00055, 0.000554 and 0.05477 ppm, respectively, indicating the  $\text{TiO}_2/\text{CQDs}/\text{CdIn}_2\text{S}_4$  photocatalyst was stable and that the photocatalytic activity derives from the whole as-prepared photocatalyst, rather than from the constituents of possible leaching.

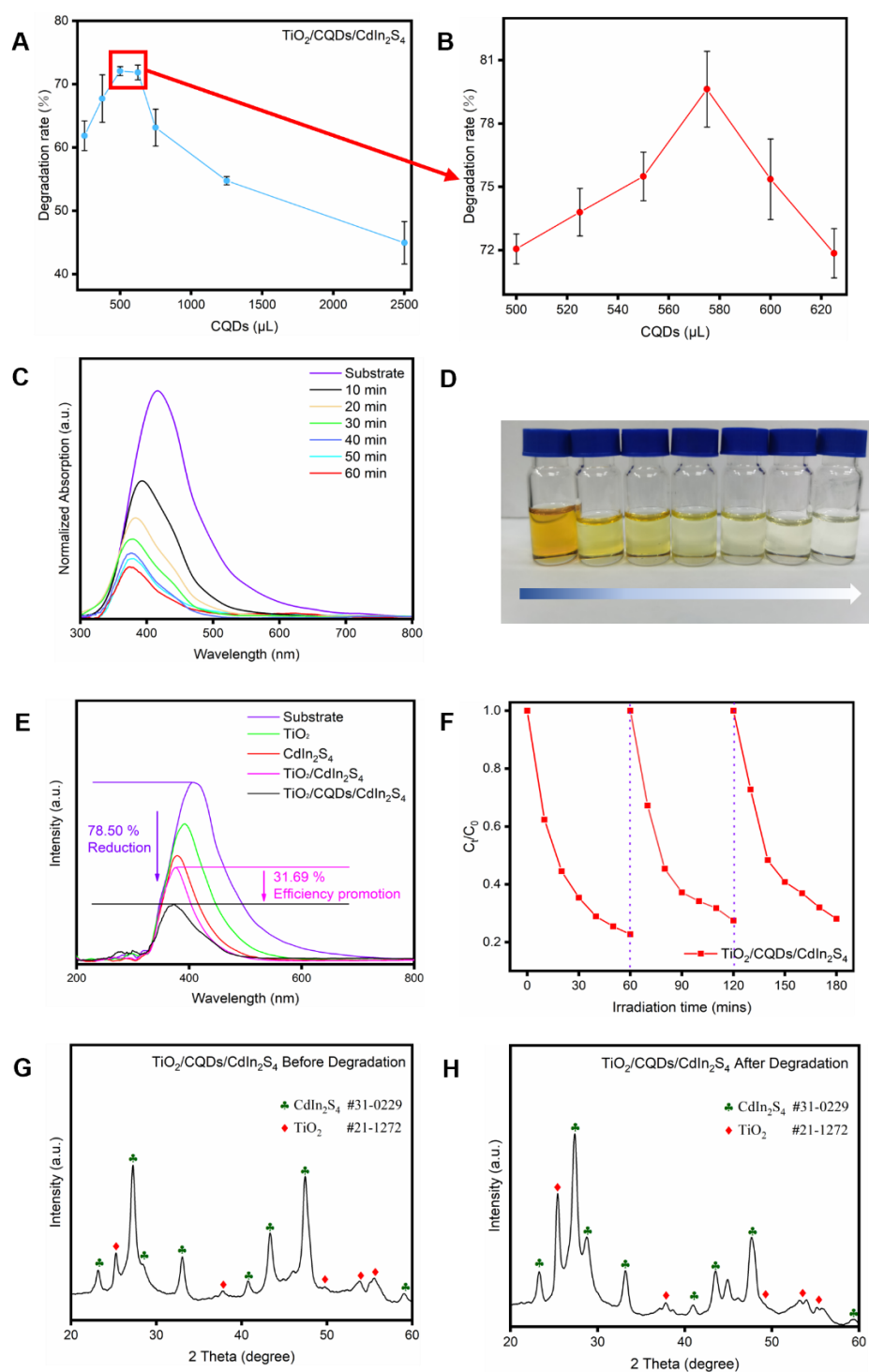


**Figure 4.** (A,B) The PAHs degradation rate by  $\text{TiO}_2/\text{CQDs}/\text{CdIn}_2\text{S}_4$  with different CQDs content; (C) UV-vis DRS of PAHs with different photocatalytic degradation time; (D) digital photograph of PAHs with different photocatalytic degradation time; (E) UV-vis DRS of PAHs degraded by different photocatalysts; (F) repeated reactions of PAHs degradation over  $\text{TiO}_2/\text{CQDs}/\text{CdIn}_2\text{S}_4$ ; (G,H) PXRD patterns of  $\text{TiO}_2/\text{CQDs}/\text{CdIn}_2\text{S}_4$  before and after 3 reaction cycles. Reaction conditions:  $100 \text{ mW cm}^{-2}$  illumination for 1 h with 50 mg photocatalyst under room temperature.

**Table 2.** Review of photocatalytic degradation performance for PAHs by varies photocatalysts.

Photocatalyst	Light Source	Weight of Photocatalyst	Amount of PAHs	Irradiation Time (min)	Degradation Efficiency (%)	Reference
TiO <sub>2</sub> TiO <sub>2</sub> /CQDs/CdIn <sub>2</sub> S <sub>4</sub>	Xe lamp (300 W) with a cutoff filter (>400 nm)	50 mg	50 mL aqueous solution, 1 mg/L	60	87.79	This work
Co <sub>3</sub> O <sub>4</sub> /Bi <sub>2</sub> O <sub>2</sub> CO <sub>3</sub>	500 W xenon lamp	25 mg	50 mL aqueous solution, 10 mg/L	150	91.02	[74]
ZnO/g-C <sub>3</sub> N <sub>4</sub>	Visible light	Not mentioned	Not mentioned	240	84.50	[75]
ZnO	15 W UVC lamp with emission at 254 nm	Not mentioned	3.5 mL of anthracene	55	60.00	[76]
CeVO <sub>4</sub> nanoparticles	Xe lamp (300 W) with a 420 nm cutoff filter	50 mg	200 mL Nap solution, 30 mg/L	60	~60.00	[77]
ZnFe <sub>2</sub> O <sub>4</sub> -CS	daylight	20 mg	5 mL aqueous solution, 2–10 mgL <sup>-1</sup>	720	95.00	[78]
TiO <sub>2</sub> -Graphene	300 W high pressure mercury lamp ( $\lambda > 320$ nm)	25 mg	250 mL aqueous solution, 0.5–5.0 $\mu$ g/mL	120	~80.00	[79]
ZnO NPs	UV lamp (368 nm, 40 W)	10 mg	50 mL aqueous solution, 23 mg/L	230	90.00	[80]

### 3.5. Photocatalytic Performance for PAHs

The obtained products were initially analyzed by FT-IR spectroscopy, as shown in Figure 5A. After degradation, the most obvious changes in FT-TR spectra are two newly appeared signals located at ca. 1260 and 1730 cm<sup>-1</sup> with high intensity, which can be assigned to the C-C key stretching vibration and aldehyde group, respectively [79,81]. In addition, increased intensity of FT-IR signals were also observed at 2860 and 2930 cm<sup>-1</sup>, which can be indexed to the cyclohexane bands [82]. These results are in good agreement with the benzaldehyde ( $m/z = 106$ ) and dimethylcyclohexane ( $m/z = 112$ ) products recorded by GC-MS (Table 3) [83]. It should be noted that the conversion rates based on GC-MS are slightly higher than that of UV-vis DRS, since some side products might not be reflected by absorption spectra. In contrast to the conversion rate of 58.42% presented by the control group without CQDs, the degradation of PAHs using the optimal TiO<sub>2</sub>/CQDs/CdIn<sub>2</sub>S<sub>4</sub>, (Figure 5B) GC-MS monitored that 87.79% of PAHs was decomposed to benzaldehyde (63.88%), dimethylcyclohexane (21.18%) and side products (2.73%) of very low proportion after 1 h of reaction.

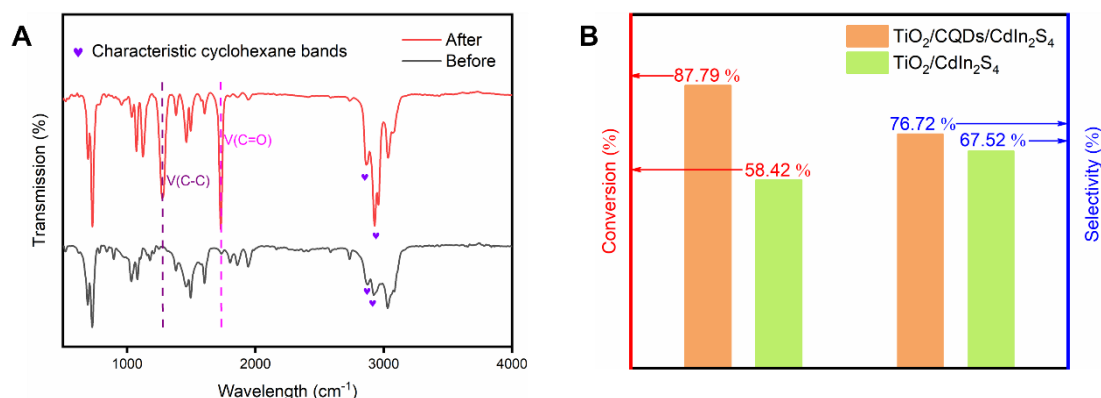


**Figure 5.** (A) FT-TR spectra of PAHs before and after the photocatalytic reactions for 1 h; (B) the performance for PAHs photocatalytic degradation over TiO<sub>2</sub>/CQDs/CdIn<sub>2</sub>S<sub>4</sub> and TiO<sub>2</sub>/CdIn<sub>2</sub>S<sub>4</sub>.

**Table 3.** GC-MS data of the main products from photocatalytic degradation of PAHs over TiO<sub>2</sub>/CQDs/CdIn<sub>2</sub>S<sub>4</sub>.

Peak	Retention Time	<i>m/z</i>	Empirical Formula	Product
2	4.472	112	C <sub>8</sub> H <sub>16</sub>	dimethylcyclohexane
3	4.565	112	C <sub>8</sub> H <sub>16</sub>	dimethylcyclohexane
4	4.743	112	C <sub>8</sub> H <sub>16</sub>	dimethylcyclohexane
5	4.859	112	C <sub>8</sub> H <sub>16</sub>	dimethylcyclohexane
6	4.938	154	C <sub>12</sub> H <sub>8</sub>	<i>acenaphthene</i>
7	5.447	106	C <sub>7</sub> H <sub>6</sub> O	<i>benzaldehyde</i>
8	5.588	106	C <sub>7</sub> H <sub>6</sub> O	<i>benzaldehyde</i>

#### 4. Conclusions

In summary, TiO<sub>2</sub>/CdIn<sub>2</sub>S<sub>4</sub> with S-Scheme band structure was modified by the introduction of CQDs during the synthetic process. Based on the in-situ XPS tests and theoretical calculations, we found that the presence of CQDs between TiO<sub>2</sub> and CdIn<sub>2</sub>S<sub>4</sub> can efficiently promote the oxidation capability of the photocatalyst, which benefits the photocatalytic degradation of PAHs. Thanks to this, the TiO<sub>2</sub>/CQDs/CdIn<sub>2</sub>S<sub>4</sub> presents outstanding photoactivity in converting the polycyclic aromatic hydrocarbons (PAHs) released by cigarettes to value-added benzaldehyde. The optimized photocatalyst performs 87.79% conversion rate and 72.76% selectivity in 1 h reaction under simulated solar source, as confirmed by FT-IR and GC-MS, which was more efficient than the control group (58.42% conversion rate).

**Supplementary Materials:** The following supporting information can be downloaded at: <https://www.mdpi.com/article/10.3390/molecules27217292/s1>, Figure S1: XRD of (a) bare CdIn<sub>2</sub>S<sub>4</sub> and (b) bare TiO<sub>2</sub>; Figure S2: The valance band edges of (a) CdIn<sub>2</sub>S<sub>4</sub> and (b) TiO<sub>2</sub>; Figure S3: (a,b) the band structure of bare CdIn<sub>2</sub>S<sub>4</sub> bulk and bare TiO<sub>2</sub> bulk, (c,d) the density of states for bare CdIn<sub>2</sub>S<sub>4</sub> bulk and bare TiO<sub>2</sub> bulk; Figure S4: EPR spectrum of (a) TiO<sub>2</sub>/CdIn<sub>2</sub>S<sub>4</sub> and (b) TiO<sub>2</sub>/CQDs/CdIn<sub>2</sub>S<sub>4</sub>; Figure S5: The elemental composition of (a) TiO<sub>2</sub>/CQDs/CdIn<sub>2</sub>S<sub>4</sub> and (b) TiO<sub>2</sub>/CdIn<sub>2</sub>S<sub>4</sub> analyzed by TEM-EDS; Figure S6: (a) HAADF TEM image of TiO<sub>2</sub>/CdIn<sub>2</sub>S<sub>4</sub> heterostructure, (b–g) respective elemental mapping of Cd, In, S, Ti and O; Figure S7: Stability of PAHs degradation of TiO<sub>2</sub>/CQDs/CdIn<sub>2</sub>S<sub>4</sub>; Figure S8: Hot filtration test of TiO<sub>2</sub>/CQDs/CdIn<sub>2</sub>S<sub>4</sub>; Table S1: Relative atomic content of TiO<sub>2</sub>/CQDs/CdIn<sub>2</sub>S<sub>4</sub> and TiO<sub>2</sub>/CdIn<sub>2</sub>S<sub>4</sub>; References [65,84].

**Author Contributions:** Conceptualization, J.Z. and F.Y.; methodology, J.Z. and M.Z.; software, X.K. and L.D.; validation, J.Z., H.Y. and M.Z.; formal analysis, J.Z. and F.Y.; investigation, J.Z. and P.G.; resources, M.Z. and D.L.; data curation, J.Z.; writing—original draft preparation, J.Z. and F.Y.; writing—review and editing, J.Z. and M.Z.; visualization, J.Z.; supervision, M.Z.; project administration, M.Z. and D.L.; funding acquisition, D.L. All authors have read and agreed to the published version of the manuscript.

**Funding:** The authors are grateful to the Guangdong Basic and Applied Basic Research Foundation (Grant NO. 2020B1515020032; 2020B1515120022), Guangzhou Basic and Applied Basic Research Foundation (Grant NO. 202201010440), the National Natural Science Foundation of China (Grant No. 62074060; 22102058) and the Science and Technology Program of Guangzhou (Grant No. 2019050001). They also acknowledge eceshi ([www.eceshi.com](http://www.eceshi.com), accessed on 3 March 2022) for the EPR analyses.

**Institutional Review Board Statement:** Not applicable.

**Informed Consent Statement:** Not applicable.

**Data Availability Statement:** All data are available in the main text or the electronic supplementary information (ESI).

**Conflicts of Interest:** The authors declare that they have no known competing financial interest or personal relationships that could have appeared to influence the work reported in this paper.

**Sample Availability:** Samples of the compounds of TiO<sub>2</sub>/CQDs/CdIn<sub>2</sub>S<sub>4</sub> and TiO<sub>2</sub>/CdIn<sub>2</sub>S<sub>4</sub> photocatalysts are available from the authors.

## References

1. Chatterjee, D.; Dasgupta, S. Visible light induced photocatalytic degradation of organic pollutants. *J. Photochem. Photobiol. C Photochem. Rev.* **2005**, *6*, 186–205. [[CrossRef](#)]
2. Chao, H.; Sun, M.; Wu, Y.; Xia, R.; Yuan, S.; Hu, F. Quantitative relationship between earthworms' sensitivity to organic pollutants and the contaminants' degradation in soil: A meta-analysis. *J. Hazard. Mater.* **2022**, *429*, 128286. [[CrossRef](#)]
3. Huang, M.; Fang, G.; Chen, N.; Zhou, D. Hydroxylamine promoted hydroxyl radical production and organic contaminants degradation in oxygenation of pyrite. *J. Hazard. Mater.* **2022**, *429*, 128380. [[CrossRef](#)]
4. Zeng, W.; Qiu, J.; Wang, D.; Wu, Z.; He, L. Ultrafiltration concentrated biogas slurry can reduce the organic pollution of groundwater in fertigation. *Sci. Total Environ.* **2022**, *810*, 151294. [[CrossRef](#)]
5. Zhan, H.; Wu, Q.; Liu, B.; Zhou, G. Exploration of Hydrogeochemical Characterization and Assessment of Organic Pollution Characteristics of Shallow Groundwater near a Chemical Plant That Discharged Sewage Illegally. *Sustainability* **2022**, *14*, 660. [[CrossRef](#)]
6. Andreoli, R.; Spatari, G.; Pigini, D.; Poli, D.; Banda, I.; Goldoni, M.; Riccelli, M.G.; Petyx, M.; Protano, C.; Vitali, M.; et al. Urinary biomarkers of exposure and of oxidative damage in children exposed to low airborne concentrations of benzene. *Environ. Res.* **2015**, *142*, 264–272. [[CrossRef](#)] [[PubMed](#)]
7. Sun, Y.; Feng, B.; Li, Q.; Tian, C.; Ma, L.; Li, Z. The Application of Bi-Doped TiO<sub>2</sub> for the Photocatalytic Oxidation of Formaldehyde. *Cryst. Res. Technol.* **2022**, *57*, 2100231. [[CrossRef](#)]
8. Han, Y.; Guo, J.; Cao, J.; Chen, C. Complexation of Triptycene-Derived Macrotricyclic Host with Bisparaquat Derivative and Self-Folding Guest: A Switchable Process Controlled by K<sup>+</sup>Ions. *Chin. J. Chem.* **2013**, *31*, 607–611. [[CrossRef](#)]
9. Huang, R.; Zhang, M.; Zheng, Z.; Wang, K.; Liu, X.; Chen, Q.; Luo, D. Photocatalytic Degradation of Tobacco Tar Using CsPbBr<sub>3</sub> Quantum Dots Modified Bi<sub>2</sub>WO<sub>6</sub> Composite Photocatalyst. *Nanomaterials* **2021**, *11*, 2422. [[CrossRef](#)] [[PubMed](#)]
10. Zhang, X.; Wang, J.; Dong, X.X.; Lv, Y.K. Functionalized metal-organic frameworks for photocatalytic degradation of organic pollutants in environment. *Chemosphere* **2020**, *242*, 125144. [[CrossRef](#)]
11. Jacob, P.; Benowitz, N.L.; Destailats, H.; Gundel, L.; Hang, B.; Martins-Green, M.; Matt, G.E.; Quintana, P.J.; Samet, J.M.; Schick, S.F.; et al. Thirdhand Smoke: New Evidence, Challenges, and Future Directions. *Chem. Res. Toxicol.* **2017**, *30*, 270–294. [[CrossRef](#)] [[PubMed](#)]
12. Shahsavari, E.; Schwarz, A.; Aburto-Medina, A.; Ball, A.S. Biological Degradation of Polycyclic Aromatic Compounds (PAHs) in Soil: A Current Perspective. *Curr. Pollut. Rep.* **2019**, *5*, 84–92. [[CrossRef](#)]
13. Ochiai, T.; Aoki, D.; Saito, H.; Akutsu, Y.; Nagata, M. Analysis of Adsorption and Decomposition of Odour and Tar Components in Tobacco Smoke on Non-Woven Fabric-Supported Photocatalysts. *Catalysts* **2020**, *10*, 304. [[CrossRef](#)]
14. Zhang, N.; Huang, C.; Tong, P.; Feng, Z.; Wu, X.; Zhang, L. Moisture stable Ni-Zn MOF/g-C<sub>3</sub>N<sub>4</sub> nanoflowers: A highly efficient adsorbent for solid-phase microextraction of PAHs. *J. Chromatogr. A* **2018**, *1556*, 37–46. [[CrossRef](#)] [[PubMed](#)]
15. Saravanan, A.; Kumar, P.S.; Jeevanantham, S.; Anubha, M.; Jayashree, S. Degradation of toxic agrochemicals and pharmaceutical pollutants: Effective and alternative approaches toward photocatalysis. *Environ. Pollut.* **2022**, *298*, 118844. [[CrossRef](#)]
16. Dai, Y.; Wang, Y.; Zuo, G.; Kong, J.; Guo, Y.; Sun, C.; Xian, Q. Photocatalytic degradation mechanism of phenanthrene over visible light driven plasmonic Ag/Ag<sub>3</sub>PO<sub>4</sub>/g-C<sub>3</sub>N<sub>4</sub> heterojunction nanocomposite. *Chemosphere* **2022**, *293*, 133575. [[CrossRef](#)]
17. Hakami, O. Construction of Co-doped NiS/S-g-C<sub>3</sub>N<sub>4</sub> heterojunction for boosting degradation of dye and inactivation of pathogens in visible light. *J. Photochem. Photobiol. A Chem.* **2022**, *425*, 113704. [[CrossRef](#)]
18. Thirukumar, P.; Atchudan, R.; Parveen, A.S.; Kalaiarasan, K.; Lee, Y.R.; Kim, S.C. Fabrication of ZnO nanoparticles adorned nitrogen-doped carbon balls and their application in photodegradation of organic dyes. *Sci. Rep.* **2019**, *9*, 19509. [[CrossRef](#)]
19. Wang, J.; Wang, T.; Zhao, Z.; Wang, R.; Wang, C.; Zhou, F.; Li, S.; Zhao, L.; Feng, M. Regulation of oxygen vacancies in SrTiO<sub>3</sub> perovskite for efficient photocatalytic nitrogen fixation. *J. Alloys Compd.* **2022**, *902*, 163865. [[CrossRef](#)]
20. Asaithambi, S.; Balaji, V.; Karuppaiah, M.; Sakthivel, P.; Muhil Eswari, K.; Yuvakkumar, R.; Selvakumar, P.; Velauthapillai, D.; Ravi, G. The electrochemical energy storage and photocatalytic performances analysis of rare earth metal (Tb and Y) doped SnO<sub>2</sub>@CuS composites. *Powder Technol.* **2022**, *33*, 103442. [[CrossRef](#)]
21. Wu, Q.; Lu, D.; Kumar Kondamareddy, K.; Ho, W.; Cao, D.; Zeng, Y.; Zhang, B.; Zhang, Y.; Xie, L.; Zhao, B.; et al. Highly efficient photocatalytic degradation for antibiotics and mechanism insight for Bi<sub>2</sub>S<sub>3</sub>/g-C<sub>3</sub>N<sub>4</sub> with fast interfacial charges transfer and excellent stability. *Arab. J. Chem.* **2022**, *15*, 103689. [[CrossRef](#)]
22. Yang, J.; Hu, C.; Jin, Y.; Chen, H.; Zhu, W.; Zhou, X. Fabrication of TiO<sub>2</sub> mesoporous microspheres sensitized with CdS nanoparticles and application in photodegradation of organic dye. *Res. Chem. Intermed.* **2018**, *47*, 3453–3468. [[CrossRef](#)]
23. Keshipour, S.; Mohammad-Alizadeh, S. Nickel phthalocyanine@graphene oxide/TiO<sub>2</sub> as an efficient degradation catalyst of formic acid toward hydrogen production. *Sci. Rep.* **2021**, *11*, 16148. [[CrossRef](#)] [[PubMed](#)]
24. Wang, S.; Liu, D.; Yu, J.; Zhang, X.; Zhao, P.; Ren, Z.; Sun, Y.; Li, M.; Han, S. Photocatalytic Penicillin Degradation Performance and the Mechanism of the Fragmented TiO<sub>2</sub> Modified by CdS Quantum Dots. *Adv. Mater.* **2021**, *6*, 18178–18189. [[CrossRef](#)] [[PubMed](#)]

25. Keshipour, S.; Khezerloo, M. Nanocomposite of hydrophobic cellulose aerogel/graphene quantum dot/Pd: Synthesis, characterization, and catalytic application. *RSC Adv.* **2019**, *9*, 17129–17136. [[CrossRef](#)]
26. Xu, W.; Tang, H.; Zhou, N.; Zhang, Q.; Peng, B.; Shen, Y. Enhanced photocatalytic activity of TiO<sub>2</sub>/Ag<sub>2</sub>O heterostructures by optimizing the separation of electric charges. *Vacuum* **2021**, *190*, 110283. [[CrossRef](#)]
27. Keshipour, S.; Mohammad-Alizadeh, S.; Razeghi, M.H. Copper phthalocyanine@graphene oxide as a cocatalyst of TiO<sub>2</sub> in hydrogen generation. *J. Phys. Chem. Solids* **2022**, *161*, 110434. [[CrossRef](#)]
28. Karuppasamy, P.; Ramzan Nilofar Nisha, N.; Pugazhendhi, A.; Kandasamy, S.; Pitchaimuthu, S. An investigation of transition metal doped TiO<sub>2</sub> photocatalysts for the enhanced photocatalytic decoloration of methylene blue dye under visible light irradiation. *J. Environ. Chem. Eng.* **2021**, *9*, 105254. [[CrossRef](#)]
29. Mahammed Shaheer, A.R.; Thangavel, N.; Rajan, R.; Abraham, D.A.; Vinoth, R.; Sunaja Devi, K.R.; Shankar, M.V.; Neppolian, B. Sonochemical assisted impregnation of Bi<sub>2</sub>WO<sub>6</sub> on TiO<sub>2</sub> nanorod to form Z-scheme heterojunction for enhanced photocatalytic H<sub>2</sub> production. *Adv. Powder Technol.* **2021**, *32*, 4734–4743. [[CrossRef](#)]
30. Mahadadalkar, M.A.; Gosavi, S.W.; Kale, B.B. Interstitial charge transfer pathways in a TiO<sub>2</sub>/CdIn<sub>2</sub>S<sub>4</sub> heterojunction photocatalyst for direct conversion of sunlight into fuel. *J. Mater. Chem. A* **2018**, *6*, 16064–16073. [[CrossRef](#)]
31. Xu, W.; Tian, W.; Meng, L.; Cao, F.; Li, L. Ion Sputtering-Assisted Double-Side Interfacial Engineering for CdIn<sub>2</sub>S<sub>4</sub> Photoanode toward Improved Photoelectrochemical Water Splitting. *Adv. Mater. Interfaces* **2020**, *7*, 1901947. [[CrossRef](#)]
32. Li, C.; Zhao, Y.; Liu, X.; Huo, P.; Yan, Y.; Wang, L.; Liao, G.; Liu, C. Interface engineering of Co<sub>9</sub>S<sub>8</sub>/CdIn<sub>2</sub>S<sub>4</sub> ohmic junction for efficient photocatalytic H<sub>2</sub> evolution under visible light. *J. Colloid Interface Sci.* **2021**, *600*, 794–803. [[CrossRef](#)] [[PubMed](#)]
33. Pei, C.-Y.; Chen, Y.-G.; Wang, L.; Chen, W.; Huang, G.-B. Step-scheme WO<sub>3</sub>/CdIn<sub>2</sub>S<sub>4</sub> hybrid system with high visible light activity for tetracycline hydrochloride photodegradation. *Appl. Surf. Sci.* **2021**, *535*, 147682. [[CrossRef](#)]
34. Zhang, Z.; Cao, Y.; Zhang, F.; Li, W.; Li, Y.; Yu, H.; Wang, M.; Yu, H. Tungsten oxide quantum dots deposited onto ultrathin CdIn<sub>2</sub>S<sub>4</sub> nanosheets for efficient S-scheme photocatalytic CO<sub>2</sub> reduction via cascade charge transfer. *Chem. Eng. J.* **2022**, *428*, 131218. [[CrossRef](#)]
35. Yang, Y.-Y.; Zhang, X.-G.; Niu, C.-G.; Feng, H.-P.; Qin, P.-Z.; Guo, H.; Liang, C.; Zhang, L.; Liu, H.-Y.; Li, L. Dual-channel charges transfer strategy with synergistic effect of Z-scheme heterojunction and LSPR effect for enhanced quasi-full-spectrum photocatalytic bacterial inactivation: New insight into interfacial charge transfer and molecular oxygen activation. *Appl. Catal. B Environ.* **2020**, *264*, 118465. [[CrossRef](#)]
36. Li, Y.; Huo, H.; Wang, X.; Xia, Y.; Zhang, A.; Gao, L. Enhancement of photocatalysis performance of CdIn<sub>2</sub>S<sub>4</sub>/g-C<sub>3</sub>N<sub>4</sub> heterojunction by H<sub>2</sub>O<sub>2</sub> synergism. *J. Mater. Sci. Mater. Electron.* **2021**, *32*, 14218–14234. [[CrossRef](#)]
37. Wang, B.; Ding, Y.; Deng, Z.; Li, Z. Rational design of ternary NiS/CQDs/ZnIn<sub>2</sub>S<sub>4</sub> nanocomposites as efficient noble-metal-free photocatalyst for hydrogen evolution under visible light. *Chin. J. Catal.* **2019**, *40*, 335–342. [[CrossRef](#)]
38. Zhao, P.; Jin, B.; Zhang, Q.; Peng, R. Facile synthesis of quantum dots/TiO<sub>2</sub> photocatalyst with superior photocatalytic activity: The effect of carbon nitride quantum dots and N-doped carbon dots. *Res. Chem. Intermed.* **2021**, *47*, 5229–5247. [[CrossRef](#)]
39. Qu, X.; Liu, M.; Yang, J.; Wang, C.; Meng, H.; Li, S.; Shi, L.; Du, F. A novel ternary TiO<sub>2</sub>/CQDs/BiOX (X = Cl, Br, I) heterostructure as photocatalyst for water purification under solar irradiation. *J. Solid State Chem.* **2018**, *264*, 77–85. [[CrossRef](#)]
40. Feng, S.; Chen, T.; Liu, Z.; Shi, J.; Yue, X.; Li, Y. Z-scheme CdS/CQDs/g-C<sub>3</sub>N<sub>4</sub> composites with visible-near-infrared light response for efficient photocatalytic organic pollutant degradation. *Sci. Total Environ.* **2020**, *704*, 135404. [[CrossRef](#)]
41. Kirbiyik Kurukavak, Ç.; Yılmaz, T.; Çetin, Ş.; Alqadasi, M.M.; Al-Khawlani, K.M.; Kuş, M. Synthesis of boron-doped CQDs and its use as an additive in P3HT:PCBM layer for efficiency improvement of organic solar cell. *Microelectron. Eng.* **2021**, *235*, 111465. [[CrossRef](#)]
42. Perdew, J.P.; Burke, K.; Ernzerhof, M. Generalized Gradient Approximation Made Simple. *Phys. Rev. Lett.* **1996**, *77*, 3865. [[CrossRef](#)] [[PubMed](#)]
43. Kresse, G.; Furthmüller, J. Efficiency of ab-initio total energy calculations for metals and semiconductors using a plane-wave basis set. *Comput. Mater. Sci.* **1996**, *6*, 15–50. [[CrossRef](#)]
44. Kresse, G.; Furthmüller, J. Efficient iterative schemes for ab initio total-energy calculations using a plane-wave basis set. *Phys. Rev. B* **1996**, *54*, 11169. [[CrossRef](#)]
45. Kresse, G.; Joubert, D. From ultrasoft pseudopotentials to the projector augmented-wave method. *Phys. Rev. B* **1999**, *59*, 1758. [[CrossRef](#)]
46. Blochl, P.E. Projector augmented-wave method. *Phys. Rev. B Condens. Matter* **1994**, *50*, 17953–17979. [[CrossRef](#)] [[PubMed](#)]
47. Ma, D.; Shi, J.W.; Zou, Y.; Fan, Z.; Shi, J.; Cheng, L.; Sun, D.; Wang, Z.; Niu, C. Multiple carrier-transfer pathways in a flower-like In<sub>2</sub>S<sub>3</sub>/CdIn<sub>2</sub>S<sub>4</sub>/In<sub>2</sub>O<sub>3</sub> ternary heterostructure for enhanced photocatalytic hydrogen production. *Nanoscale* **2018**, *10*, 7860–7870. [[CrossRef](#)] [[PubMed](#)]
48. Huang, J.; Li, L.; Chen, J.; Ma, F.; Yu, Y. Broad spectrum response flower spherical-like composites CQDs@CdIn<sub>2</sub>S<sub>4</sub>/CdS modified by CQDs with up-conversion property for photocatalytic degradation and water splitting. *Int. J. Hydrogen Energy* **2020**, *45*, 1822–1836. [[CrossRef](#)]
49. Li, Y.; Li, L.; Dong, X.; Xin, Z.; Guan, J.; Gao, X.; Zu, W.; Zhang, W. Minimalist preparation and photocatalysis properties of a spinyball-like indium-based composite suitable for different light conditions. *J. Alloys Compd.* **2022**, *909*, 164701. [[CrossRef](#)]
50. Ding, J.; Yan, W.; Sun, S.; Bao, J.; Gao, C. Hydrothermal synthesis of CaIn<sub>2</sub>S<sub>4</sub>-reduced graphene oxide nanocomposites with increased photocatalytic performance. *ACS Appl. Mater. Interfaces* **2014**, *6*, 12877–12884. [[CrossRef](#)]

51. Luo, D.; Chen, Q.; Qiu, Y.; Liu, B.; Zhang, M. Carbon Dots-Decorated Bi<sub>2</sub>WO<sub>6</sub> in an Inverse Opal Film as a Photoanode for Photoelectrochemical Solar Energy Conversion under Visible-Light Irradiation. *Materials* **2019**, *12*, 1713. [[CrossRef](#)] [[PubMed](#)]
52. Sharma, S.; Mehta, S.K.; Ibhaddon, A.O.; Kansal, S.K. Fabrication of novel carbon quantum dots modified bismuth oxide (alpha-Bi<sub>2</sub>O<sub>3</sub>/C-dots): Material properties and catalytic applications. *J. Colloid Interface Sci.* **2019**, *533*, 227–237. [[CrossRef](#)] [[PubMed](#)]
53. Biswal, R.; Khan, B.; Singh, M.K. Synthesis, optical, dielectric, and magneto-dielectric properties of graphene quantum dots (GQDs). *J. Mater. Res.* **2022**, 1–11. [[CrossRef](#)]
54. Sharma, D.; Malik, B.P.; Gaur, A. Pulsed laser induced optical nonlinearities in undoped, copper doped and chromium doped CdS quantum dots. *J. Opt.* **2015**, *17*, 045502. [[CrossRef](#)]
55. Yadav, I.; Ahlawat, D.S.; Ahlawat, R. Cu-doped Cd<sub>1-x</sub>Zn<sub>x</sub>S alloy: Synthesis and structural investigations. *Appl. Phys. A* **2016**, *122*, 245. [[CrossRef](#)]
56. Zhang, X.; Hou, S.; Mao, H.; Wang, J.; Zhu, Z. Influence of annealing temperature on the photoluminescence properties of ZnO quantum dots. *Appl. Surf. Sci.* **2010**, *256*, 3862–3865. [[CrossRef](#)]
57. Peng, Z.; Jiang, Y.; Wang, X.; Zhang, R.; Xu, H.; Xiao, Y.; Jing, X.; Zhang, J.; Liu, Y.; Ni, L. Novel CdIn<sub>2</sub>S<sub>4</sub> nano-octahedra/TiO<sub>2</sub> hollow hybrid heterostructure: In-situ synthesis, synergistic effect and enhanced dual-functional photocatalytic activities. *Ceram. Int.* **2019**, *45*, 15942–15953. [[CrossRef](#)]
58. Hu, J.; Yang, M.; Ke, X.; Yang, S.; Wang, K.; Huang, H.; Wang, W.; Luo, D.; Zheng, Z.; Huang, L.; et al. Cubic-cubic perovskite quantum dots/PbS mixed dimensional materials for highly efficient CO<sub>2</sub> reduction. *J. Power Sources* **2021**, *481*, 228838. [[CrossRef](#)]
59. Bae, H.-S.; Patil, R.P.; Chae, W.-S.; Ryu, J.; Mahadik, M.A.; Jang, J.S. Morphology control and phase transformation of ZIS/TiO<sub>2</sub> into CdSe(en)<sub>0.5</sub>/CIS/TiO<sub>2</sub> photoanode for enhanced solar hydrogen generation. *Chem. Eng. J.* **2020**, *385*, 123871. [[CrossRef](#)]
60. Zhao, X.; Zhou, Y.; Liang, Q.; Zhou, M.; Li, Z.; Xu, S. Coupling MOF-derived titanium oxide with CdIn<sub>2</sub>S<sub>4</sub> formed 2D/3D core-shell heterojunctions with enhanced photocatalytic performance. *Sep. Purif. Technol.* **2021**, *279*, 119765. [[CrossRef](#)]
61. Karthik, R.; Vinoth Kumar, J.; Chen, S.M.; Karuppiyah, C.; Cheng, Y.H.; Muthuraj, V. A Study of Electrocatalytic and Photocatalytic Activity of Cerium Molybdate Nanocubes Decorated Graphene Oxide for the Sensing and Degradation of Antibiotic Drug Chloramphenicol. *ACS Appl. Mater. Interfaces* **2017**, *9*, 6547–6559. [[CrossRef](#)] [[PubMed](#)]
62. Cao, X.; Huang, A.; Liang, C.; Chen, H.C.; Han, T.; Lin, R.; Peng, Q.; Zhuang, Z.; Shen, R.; Chen, H.M.; et al. Engineering Lattice Disorder on a Photocatalyst: Photochromic BiOBr Nanosheets Enhance Activation of Aromatic C-H Bonds via Water Oxidation. *J. Am. Chem. Soc.* **2022**, *144*, 3386–3397. [[CrossRef](#)] [[PubMed](#)]
63. Sundaresan, P.; Karthik, R.; Chen, S.M.; Vinoth Kumar, J.; Muthuraj, V.; Nagarajan, E.R. Ultrasonication-assisted synthesis of sphere-like strontium cerate nanoparticles (SrCeO<sub>3</sub> NPs) for the selective electrochemical detection of calcium channel antagonists nifedipine. *Ultrason. Sonochem.* **2019**, *53*, 44–54. [[CrossRef](#)] [[PubMed](#)]
64. Poolwong, J.; Del Gobbo, S.; D'Elia, V. Transesterification of dimethyl carbonate with glycerol by perovskite-based mixed metal oxide nanoparticles for the atom-efficient production of glycerol carbonate. *J. Ind. Eng. Chem.* **2021**, *104*, 43–60. [[CrossRef](#)]
65. Li, X.; Kang, B.; Dong, F.; Zhang, Z.; Luo, X.; Han, L.; Huang, J.; Feng, Z.; Chen, Z.; Xu, J.; et al. Enhanced photocatalytic degradation and H<sub>2</sub>/H<sub>2</sub>O<sub>2</sub> production performance of S-pCN/WO<sub>2.72</sub> S-scheme heterojunction with appropriate surface oxygen vacancies. *Nano Energy* **2021**, *81*, 105671. [[CrossRef](#)]
66. Xu, Q.; Zhang, L.; Cheng, B.; Fan, J.; Yu, J. S-Scheme Heterojunction Photocatalyst. *Chem* **2020**, *6*, 1543–1559. [[CrossRef](#)]
67. Chen, P.; Zhang, H.; Tang, P.; Li, B. A hybrid density functional design of intermediate band semiconductor for photovoltaic application based on group IV elements (Si, Ge, Sn, and Pb)-doped CdIn<sub>2</sub>S<sub>4</sub>. *J. Appl. Phys.* **2022**, *131*, 135702. [[CrossRef](#)]
68. Wang, H.; Xia, Y.; Li, H.; Wang, X.; Yu, Y.; Jiao, X.; Chen, D. Highly active deficient ternary sulfide photoanode for photoelectrochemical water splitting. *Nat. Commun.* **2020**, *11*, 3078. [[CrossRef](#)]
69. Qu, Z.; Su, Y.; Sun, L.; Liang, F.; Zhang, G. Study of the Structure, Electronic and Optical Properties of BiOI/Rutile-TiO<sub>2</sub> Heterojunction by the First-Principle Calculation. *Materials* **2020**, *13*, 323. [[CrossRef](#)]
70. Galinato, M.G.; Niedzwiedzki, D.; Deal, C.; Birge, R.R.; Frank, H.A. Cation radicals of xanthophylls. *Photosynth Res.* **2007**, *94*, 67–78. [[CrossRef](#)]
71. Kumar, A.; Sharma, S.K.; Sharma, G.; Al-Muhtaseb, A.H.; Naushad, M.; Ghfar, A.A.; Stadler, F.J. Wide spectral degradation of Norfloxacin by Ag@BiPO<sub>4</sub>/BiOBr/BiFeO<sub>3</sub> nano-assembly: Elucidating the photocatalytic mechanism under different light sources. *J. Hazard. Mater.* **2019**, *364*, 429–440. [[CrossRef](#)] [[PubMed](#)]
72. Liu, C.; Abbaspour, S.; Rouki, M.; Tayebee, R.; Jarrahi, M.; Shahri, E.E. Synergistic promotion of the photocatalytic efficacy of CuO nanoparticles by heteropolyacid-attached melem: Robust photocatalytic efficacy and anticancer performance. *Appl. Organomet. Chem.* **2022**, *36*, e6878. [[CrossRef](#)]
73. El-Shabasy, R.; Yosri, N.; El-Seedi, H.; Shoueir, K.; El-Kemary, M. A green synthetic approach using chili plant supported Ag/AgO@P25 heterostructure with enhanced photocatalytic properties under solar irradiation. *Optik* **2019**, *192*, 162943. [[CrossRef](#)]
74. Guo, Y.; Dai, Y.; Zhao, W.; Li, H.; Xu, B.; Sun, C. Highly efficient photocatalytic degradation of naphthalene by Co<sub>3</sub>O<sub>4</sub>/Bi<sub>2</sub>O<sub>2</sub>CO<sub>3</sub> under visible light: A novel p-n heterojunction nanocomposite with nanocrystals/lotus-leaf-like nanosheets structure. *Appl. Catal. B Environ.* **2018**, *237*, 273–287. [[CrossRef](#)]
75. Mukwevho, N.; Kumar, N.; Fosso-Kankeu, E.; Waanders, F.; Bunt, J.; Ray, S.S. Visible light-excitable ZnO/2D graphitic-C<sub>3</sub>N<sub>4</sub> heterostructure for the photodegradation of naphthalene. *Desalination Water Treat.* **2019**, *163*, 286–296. [[CrossRef](#)]

76. Martínez-Vargas, B.L.; Díaz-Real, J.A.; Reyes-Vidal, Y.; Rodríguez-López, J.L.; Ortega Borges, R.; Ortiz-Frade, L. Competition between the reaction medium and nanostructured ZnO in the photocatalytic degradation of anthracene. Toward an optimal process for polycyclic aromatic hydrocarbons remediation. *Química Nova* **2017**, *40*, 6–16. [[CrossRef](#)]
77. Lu, G.; Song, B.; Li, Z.; Liang, H.; Zou, X. Photocatalytic degradation of naphthalene on CeVO<sub>4</sub> nanoparticles under visible light. *Chem. Eng. J.* **2020**, *402*, 125645. [[CrossRef](#)]
78. Rani, M.; Rachna; Shanker, U. Metal oxide-chitosan based nanocomposites for efficient degradation of carcinogenic PAHs. *J. Environ. Chem. Eng.* **2020**, *8*, 103810. [[CrossRef](#)]
79. Bai, H.; Zhou, J.; Zhang, H.; Tang, G. Enhanced adsorbability and photocatalytic activity of TiO<sub>2</sub>-graphene composite for polycyclic aromatic hydrocarbons removal in aqueous phase. *Colloids Surf. B Biointerfaces* **2017**, *150*, 68–77. [[CrossRef](#)]
80. Sliem, M.A.; Salim, A.Y.; Mohamed, G.G. Photocatalytic degradation of anthracene in aqueous dispersion of metal oxides nanoparticles: Effect of different parameters. *J. Photochem. Photobiol. A Chem.* **2019**, *371*, 327–335. [[CrossRef](#)]
81. Kozlov, D.V.; Paukshtis, E.A.; Savinov, E.N. The comparative studies of titanium dioxide in gas-phase ethanol photocatalytic oxidation by the FTIR in situ method. *Appl. Catal. B Environ.* **2000**, *24*, 7–12. [[CrossRef](#)]
82. Zheng, C.; Li, X.; Zhao, Q.; Qu, Z.; Quan, X. Photo-oxidation of gas-phase cyclohexane species over nanostructured TiO<sub>2</sub> fabricated by different strategies. *Sep. Purif. Technol.* **2009**, *67*, 326–330. [[CrossRef](#)]
83. Chen, L.; Guo, F.; Wu, J.; Li, P.; Zhang, Y. Research on Coal Tar Pitch Catalytic Oxidation and Its Effect on the Emission of PAHs during Co-Carbonation with Coal. *Catalysts* **2021**, *11*, 1428. [[CrossRef](#)]
84. Li, Y.; Wang, K.; Huang, D.; Li, L.; Tao, J.; Ghany, N.A.A.; Jiang, F. Cd<sub>x</sub>Zn<sub>1-x</sub>S/Sb<sub>2</sub>Se<sub>3</sub> thin film photocathode for efficient solar water splitting. *Appl. Catal. B Environ.* **2021**, *286*, 119872. [[CrossRef](#)]